Published in final edited form as:
Methods. 2012 February ; 56(2): 310–316. doi:10.1016/j.ymeth.2011.08.017.

Optimization of Immunolabeled Plasmonic Nanoparticles for Cell Surface Receptor Analysis

Kevin Seekell[1], **Hillel Price**[1], **Stella Marinakos**[2], and **Adam Wax**[1]

[1]Department of Biomedical Engineering, Fitzpatrick Institute for Photonics Duke University, Durham, NC 27708

[2]Center for the Environmental Implications of NanoTechnology, Duke University, Durham, NC 27708

Abstract

Noble metal nanoparticles hold great potential as optical contrast agents due to a unique feature, known as the plasmon resonance, which produces enhanced scattering and absorption at specific frequencies. The plasmon resonance also provides a spectral tunability that is not often found in organic fluorophores or other labeling methods. The ability to functionalize these nanoparticles with antibodies has led to their development as contrast agents for molecular optical imaging. In this review article, we present methods for optimizing the spectral agility of these labels. We discuss synthesis of gold nanorods, a plasmonic nanoparticle in which the plasmonic resonance can be tuned during synthesis to provide imaging within the spectral window commonly utilized in biomedical applications. We describe recent advances in our group to functionalize gold and silver nanoparticles using distinct antibodies, including EGFR, HER-2 and IGF-1, selected for their relevance to tumor imaging. Finally, we present characterization of these nanoparticle labels to verify their spectral properties and molecular specificity.

Keywords

Plasmonic nanoparticles; cell imaging; microscpectroscopy; darkfield microscopy

1. Introduction

Nanoparticles hold great promise for application to biomedicine due to their nanoscale size, which confers unique characteristics. Nanoscale metallic structures display distinct optical characteristics not seen at either the macro or atomic scale. Specifically, the optical properties of nano-scale metals are not solely dependent on their composition, but also depend on their specific geometry [1–3]. The implications of this aspect are vast, as the extinction characteristics of metal nanoparticles may be finely adjusted by synthesizing particles of different sizes or shapes. Nobel metal nanoparticles are known to scatter and absorb strongly at specific wavelengths due to their localized surface plasmon resonance, an effect in which oscillating electrons are confined by the nanoscale dimensions of the particle. The ability to target a narrow region of the optical spectrum has led to significant research on the use of plasmonic nanoparticles for molecular optical imaging.

Plasmonic nanoparticles, offer significant advantage over other labeling agents. For example, they offer greater photostability than fluorescent agents [4–6], and increased solubility in water and lower cytotoxicity than quantum dots [7, 8]. Application of plasmonic nanoparticles can be somewhat limited due to their larger size, as compared to fluorescent dyes, providing a practical limit on the concentration delivered to cells and tissues. Upon antibody conjugation, immunolabeled plasmonic nanoparticles can be used to target specific molecules for sensing [9–14] and imaging [15–21] applications.

Plasmonic nanoparticles can be employed to target specific molecules through immunolabelling, with the plasmon resonance providing an effective mechanism to generate optical contrast [15–21]. The increase in scattering and absorption due to this resonance is highly wavelength specific and can be tuned by changing the material or confirmation of the particles. Geometries such as gold nanospheres [22, 23], nanorods [24, 25], nanoshells [19, 20, 26, 27], and nanostars [28, 29] have been developed, each with their own distinct spectral properties. While commercially available gold and silver nanospheres can cover a good portion of the visible spectrum, the use of the plasmonic gold nanorod (GNR) has provided access to a unique spectral window in the near infrared, that is highly desirable for biomedical imaging [3]. Optical excitation in the region between 700 and 900 nm is often termed the therapeutic window, for its low absorption in water and hemoglobin. Thus, GNR's provide a suitable contrast agents for optical imaging techniques that exploit this window for excitation such as optical coherence tomography [30, 31], and diffuse optical tomography [27].

In the following, we will review several key methods for providing spectral agility of immunolabeled plasomonic nanoparticles. We will review the synthesis of GNR's and experimentally characterize their tunability in the red to near infrared region. We then present several conjugation protocols for immunolabelling three different species of nanoparticles using three different receptor antibodies that are relevant for cancer imaging, including GNR's targeted to epidermal growth factor receptor (EGFR), commercially available gold nanopsheres targeted to human epidermal growth factor receptor 2 (HER-2) and commercially available silver nanospheres targeted to insulin like growth factor 1 (IGF-1R). We then present experimental results which demonstrate molecular specific binding, compared controls including nanoparticles conjugated to non-specific IgG antibody, obtained using a darkfield microspectroscopy system.

2. Materials and Methods

2.1 Gold Nanorod Synthesis

Gold nanorods were synthesized using an adaptation of seed-mediated methods developed by Nikoobakht et al [25]. A seed solution was created by first adding 0.250 mL of 0.01M hydrogen tetrachloroaurate trihydrate ($HAuCl_4 \cdot 3H_2O$, Sigma-Aldrich, 520918) to 7.5mL of an aqueous solution of 0.1M hexadecyltrimethylammonium bromide (CTAB, Sigma-Aldrich, H9151). Gold seeds were then formed by adding 0.6 mL of cold 0.01M sodium borohydride ($NaBH_4$, Alfa Aesar, 13432), a strong reducing agent. This solution was gently stirred and heated until it was ready for use in nanorod synthesis.

The gold nanorod solution was formed by first adding 4 mL of 0.01M $HAuCl_4$ to 95 mL of 0.1M CTAB in a separate bottle kept at 29°C in a water bath. The addition of this acid changes the CTAB solution's appearance from clear to yellow. 0.01 M silver nitrate ($AgNO_3$, Alfa-Aesar, 11414) was added to the resulting solution. The exact amount of silver nitrate added was varied for each sample (150–290 μL) to control the nanorods' aspect ratio and peak resonant wavelength. 0.64 mL of 0.1M ascorbic acid ($C_6H_8O_6$, Alfa-Aesar, 11188), a weak reducing agent, was then added, changing the color of the solution from

yellow to clear. After adding each of these components, the bottle was swirled to ensure even mixing. Finally, 50 uL of the previously described gold seed solution was added to the solution to begin nanorod formation. The bottle was immediately capped and inverted 5 times to evenly mix the seed. The solution was then left overnight in the water bath to react.

2.2 Gold Nanorod Characterization

After overnight incubation, the NP's were characterized using a UV-VIS spectrophotometer (Cary 300 Bio). The extinction spectra of GNR solution diluted 50:50 with DI water were measured from 400–800 nm at 1 nm intervals. The longitudinal peak resonance wavelength and corresponding 95% confidence interval were determined by fitting the portion of the extinction spectra within 50 nm of the measured maximum extinction value to a Gaussian function.

Size distributions of each batch of nanorods were measured using a transmission electron microscope (FEI Tecnai G^2 Twin). Samples were prepared by placing a 10 μL drop of nanorod solution onto a formvar-coated copper TEM grid with a carbon film (FCF200-Cu, Electron Microscopy Sciences). The rods were allowed to settle on the grid for 15 minutes before gently removing the excess fluid with a tissue. Grids were then placed in the TEM for imaging.

Gold nanorods were imaged under the TEM at 160 kV and 80 kX magnification. At least 90 particles were imaged from each batch. The length and width of each particle were measured, allowing for the calculation of the particle's aspect ratio (R=length/width). The measurements from all of the individual particles are analyzed to determine size distributions for each batch in length, width, and aspect ratio. This information may be used to theoretically simulate the absorption and scattering coefficients of the nanorods, and compare them to the experimentally obtained results.

Furthermore, the concentration of the nanorod solution may be estimated using the average dimensions obtained from the TEM. Assuming that the rods are cylindrical in shape, their approximate volume may be easily calculated using the measured average length and width. Multiplying the number of moles of Au used in the synthesis procedure by molar volume of Au (10.21 cm^3/mol) results in the total volume of gold in the solution. Assuming that all of the gold used is converted into nanorods, dividing the total volume of Au by the volume of a single rod estimates the total number of GNRs in the solution, and therefore the concentration.

2.3 Antibody-NP Conjugation

Gold nanorods were conjugated according to published procedures[32, 33] with anti-EGFR (E2156, clone 225, Sigma-Aldrich, St. Louis, MO, 1.56 mg/mL stock solution) or with mouse IgG1 κ isotype control (16-4714-85, eBioscience, 1.54 mg/mL stock solution) as a negative control. 1 mL of the gold nanorod suspension was centrifuged twice (10,000 RPM for 5 min.) and resuspended in 1 mL of 1 mM NaCl. Polystyrene sulfonate (200 μL, 10 mg/mL in 1 mM NaCl, MW 18,000, Polysciences, Inc.) was added to the nanorods, and the suspension was placed on a shaker for 20 min. The nanorods were centrifuged at 10,000 RPM for 5 min. and resuspended in 1 mL of 20 mM HEPES pH 7.4. Four μL of 1.56 mg/mL mouse monoclonal anti-EGFR were added, and the suspension was placed on an oscillator for 30 min. The nanorods were centrifuged at 10,000 RPM for 5 min. and then finally resuspended in 0.5 mL of PBS containing 5 mg/mL BSA.

Anti-IGF-1R nanosphere conjugates consist of 0.5 mL of 100 nm diameter silver colloid (15709-20SC, Ted Pella, Inc., Redding, CA) solution diluted with 485 μL of 20 mM HEPES buffer and 16.1 μL of 1.40 mg/mLanti-IGF-1R (MS-301-PABX, ABD Serotec, Raleigh,

NC) solution diluted with 62.5 μL of 20 mM HEPES buffer. HER-2 Ab nanosphere conjugates consist of 0.5 mL of 60 nm diameter Au colloid (15709-20, Ted Pella, Inc., Redding, CA) solution diluted with 485 μL of 20 mM HEPES buffer and 14.4 μL of 1.04 mg/mL HER-2 Ab (MS-301-PABX, Labvision, Fremont, CA) solution diluted with 62.5 μL of 20 mM HEPES buffer. Both conjugates were prepared using identical procedures. 100 nM K_2CO_3 was used to adjust the pH of each solution to 7.0 ± 0.2. Solutions were then mixed on an oscillator for 20 minutes at 190 cycles/min. Following mixing, the solution was tested for antibody-nanoparticle conjugation by removing 100 μL and subsequent addition of 5 μL of 10% NaCl. Incomplete antibody coverage would result in a bluish color change due to particle aggregation. To prevent non-specific binding of proteins to remaining NP surface, 100 μL of 1% PEG (P2263, Sigma-Aldrich, St. Louis, MO) was added to the suspension and then allowed to interact. 15 minutes of centrifuging at 6000 RPM was used to remove excess PEG. Supernatant was removed, and the NP pellet was resuspended with 0.5 ml of PBS. These steps were then repeated to ensure complete removal of PEG, with minimal removal of NPs. This protocol is an adaptation of methods developed by the Drezek, Richards-Kortum, and Sokolov groups[16, 17, 32, 34].

2.4 Cell-NP Treatment

For each cell line used, 80k cells were plated on chambered cover glasses and incubated overnight. The cell media was then removed and replaced by 0.5 ml PBS/5% FBS and 0.5 mL of antibody-GNR solution. Cells were then incubated in the GNR solution for 20 minutes, allowing sufficient time for binding between antibodies and targeted receptors. Finally, the GNR solution was removed, and cells were washed with media twice before imaging.

2.5 Darkfield Hyperspectral Microscopy

Cells were imaged using a custom built darkfield hyperspectral imaging system [32]. Light from a super-continuum light source (Fianium) was passed through an acousto-optical tunable filter (AOTF), which may be tuned to filter any wavelength in the visible region (bandwidth of 3.5 nm at 515 nm). The filtered light then passes through a custom epi-darkfield illumination train before reaching the cells[35]. The darkfield optics ensures that only scattered light is imaged. Epi-illumination ensures that the forward scattering caused by the bulk volume of the cells is minimal, as opposed to the case for transmission darkfield imaging, where cell scattering can be substantial. Scattered light is then collected and sent to a CCD camera (Cascade 650, Photometrics) for imaging. The result is a high contrast image of the scattered light from bound NPs with negligible contributions from the cell.

Hyperspectral data cubes were built by taking images from 450–700 nm with an integration time of 30 ms per image. This integration time was minimized by imaging the cells with a 170×170 pixel area. Data sets were acquired either in 1 nm or 5 nm intervals, resulting in total image acquisition times of ~2.4s or 12.0s, respectively. Scattering spectra were calculated by averaging the intensity over the 170×170 pixel area for each wavelength. Source-correction is performed by normalizing the obtained signal by source intensity, which is determined by using a diffuse reflectance standard (WS-1, Ocean Optics, Dunedin, FL).

3. Theory

3.1 Local Surface Plasmon Resonance

The enhanced absorption and scattering characteristics of gold nanoparticles arise from a process known as Local Surface Plasmon Resonance (LSPR). LSPR may be understood by considering the interactions between an EM-wave and the atomic structure of a gold

particle. As is the case with all metals, the conduction band electrons of gold are not bound to any specific atom, and are allowed to move freely through the material. The mean free path of an electron in gold is approximately 50 nm [36]. In particles with dimensions in this range, electrons can move throughout the entire material without any scattering. Therefore, interactions with the EM-wave may be considered only at the particle's surface.

When an EM-wave interacts with a nanoparticle that is of smaller dimension than the wavelength, it causes resonant oscillations of the particle's free electrons [1, 36]. These oscillations are known as surface plasmons. The decay of the surface plasmon causes the nanoparticles' enhanced optical properties. Non-radiative plasmon decay results in enhanced absorption while radiative plasmon decay results in enhanced scattering [37]. This scattering is completely elastic (i.e. scattered photons retain their initial wavelength) [38]. The ability of the nanoparticle's electrons to effectively resonate with the EM-wave, and therefore absorb and scatter, is a function of the excitation wavelength. Research has shown that the peak resonant wavelength of a nanoparticle is dependent on its size, shape, composition, and the surrounding dielectric environment [1–3]. By adjusting these parameters, particles may be synthesized with peak absorbing and scattering wavelengths extending from the visible to near infrared ranges. For example, silver nanospheres can scatter light from 400–500 nm while gold nanospheres predominantly scatter light from 500–600 nm. This range is further extended by gold nanorods, which can be adjusted with peak resonant wavelengths anywhere between 600–2200 nm [14].

3.2 DDA Simulations of Gold Nanorods

The absorption and scattering properties of spherical nanoparticles may be easily calculated using Mie theory. However, Mie theory fails to predict the properties of non-symmetric nanoparticles, such as nanorods. More complex approximations are required to determine the optical properties of particles with complex geometries.

Discrete Dipole Approximation (DDA) is an accurate method of determining the absorption and scattering properties of particles with arbitrary geometries[39]. Briefly, this algorithm replaces a continuous material with a number of discrete polarizable dipoles. Each dipole is affected by the external electric field as well as the fields produced by the surrounding dipoles. DDA calculates the response of all of the individual dipoles within the specified geometry to determine absorption and scattering coefficients. The overall accuracy of this approximation increases along with the number of dipoles used. However, calculating the response of an excessive number of dipoles is computationally demanding.

Figure 1 shows the extinction spectra of four GNR geometries calculated using DDSCAT 7.1 software [40]. The geometry of the GNRs is assumed to be cylinders terminating with hemispherical caps on either end. Shapes were varied by extending the overall length of the rod while keeping the width constant. This varies the aspect ratio of the GNR (length/width). These simulations provide two important insights concerning the optical properties of GNRs. First, unlike nanospheres, GNRs exhibit two resonance peaks, one smaller peak near 520 nm and a second, larger red-shifted peak. These two distinct peaks relate to the asymmetry of the GNR. The blue-shifted peak corresponds to the rod's short (transverse) axis, while the red-shifted peak corresponds to the long (longitudinal) axis [24]. In fact, excitation of these two resonant peaks is dependent on the polarization of the incoming light [41]. For example, light polarized parallel to the long axis excites resonant oscillations corresponding to the longitudinal peak resonant wavelength, while having no effect on the transverse peak resonance. In most applications, both peaks are observed as natural light is randomly polarized.

A second note of interest regarding these simulations is the effect of a GNR's aspect ratio on the longitudinal peak resonance wavelength. As the rod's length is extended, the peak extinction both increases in amplitude and red-shifts in wavelength. Simulations and experimental data have shown that there is a linear relationship between a GNR's aspect ratio and its peak resonant wavelength [3, 24]. The longitudinal peak resonance can extend anywhere from 600 nm to 2200 nm [14]. This large range allows for the use of GNRs in many applications using both visible and NIR light. It is also possible to use multiple types of GNRs for multiplexed sensing if their absorption or scattering peaks are well separated. In this study, we will demonstrate the ability to finely tune the aspect ratios of GNR's to vary the absorption peaks across the 600–700 nm range.

4. Results

4.1 Nanoparticle Synthesis

Eight batches of GNRs were synthesized using the seed-mediated method described above. Each batch was made with a different volume of silver nitrate ranging from 150 to 290 μL. Figure 2 shows two representative TEM images of GNRs synthesized with 170 and 290 μL of silver nitrate, respectively. The addition of silver nitrate facilitates growth in the longitudinal direction, resulting in an increased average aspect ratio. A possible mechanism for this effect will be discussed in Section 5. Using the calculations described above, the concentrations of the GNR solutions range from 7.87e-11 to 1.27e-10 M.

Figure 3(a) emphasizes the role of the mean aspect ratio in determining the optical properties of GNRs. As the aspect ratio increases, the longitudinal peak resonant wavelength red-shifts, and increases in amplitude, as predicted by DDA simulations. Note that when the mean aspect ratio is relatively low ($R<1.5$), the longitudinal and transverse peak resonant wavelengths are not sufficiently spaced apart to completely differentiate the two. The shift in the absorption characteristics may be observed visually, as the color of the GNR solution shifts from purple to blue as the absorption peak redshifts through the 600–700 nm region.

Figures 3(b–d) demonstrate the ability to tune the aspect ratio, and therefore the peak resonance wavelength, by adjusting the amount of $AgNO_3$ added during seed-mediated synthesis. The peak wavelength does not show dependence when low amounts of $AgNO_3$ are used. However, at amounts greater than 230 μL of $AgNO_3$, a linear relationship develops between these two variables. The linear region extends from 610 nm to at least 680 nm. These characterization experiments confirm a simple method of adjusting the resonance peak wavelength of GNR's by adjusting the amount of silver nitrate added. The outlier at 210 nm is believed to be the result of a slight error in the volume of one of the chemical components during synthesis. The seed-mediated synthesis method has proven to be quite sensitive to the concentrations of each compound.

A similar relationship is noted between the average GNR aspect ratio and the amount of $AgNO_3$ used. Again, small deviations are observed at low $AgNO_3$ concentrations, leading to an approximately linear relationship for amounts greater than 230 μL $AgNO_3$. The results from these two plots suggest a strong correlation between the GNRs' resonant peak wavelength and aspect ratio. Figure 3(d) displays a linear relationship between these two factors. This result agrees with DDA simulations, suggesting that the average aspect ratio, and therefore the resonance peak, may be finely tuned using these methods.

4.2 Confirmation of molecular specificity

Experiments were performed to demonstrate the molecular specificity of each of the three labels described above. The anti-EGFR gold nanorod conjugation protocol was verified with MDA-MB-468 human breast adenocarcinoma. These cells were confirmed to over-express

EGFR[42] using ELISA and found to have 5.60 ng/ml, approximately 5× that of control cell lines (A549, MDA-MB-453). The MDA-MB-468 cells were incubated with the anti-EGFR gold nanorod conjugates and hyperspectral data cubes were acquired for individual cells using the hyperspectral microscopy system described above. Scattering spectra were averaged over each cell to assess the signal arising from the labeling and the total signal was calculated for N=139 cells.). Spectral measurements determine an average peak scattering wavelength of 664.0±9.3 nm for these cells [32].

Controls consisted of exposure of EGFR non-expressing MDA-MB-453 human breast carcinoma cells to anti-EGFR nanorod conjugates, [43, 44] EGFR expressing MDA-MB-468 cells exposed to IgG1 Ab labeled gold nanorods, and MDA-MB-468 cells not exposed to any labels. Control experiments showed negligible increases in scattering, demonstrating statistically significant differences in scattering intensity from the labeled, expressing cells ($p < 0.001$) and confirming molecular specificity (Figure 4).

Experiments were also performed to demonstrate the molecular specificity of the anti-IGF-1R silver nanosphere conjugation protocol. A549 human alveolar adenocarcinoma cells were confirmed to over-express IGF-1R [43, 45] using ELISA and found to have 0.352 ng/ml, approximately 4× that of control cells (MDA-MB-468). A549 cells were exposed to the anti-IGF-1R conjugates and hyperspectral data cubes were acquired for individual cells using the hyperspectral microscopy system. Scattering spectra were acquired for several cells (N=102) and used to assess the average scattering. Spectral measurements determine an average peak scattering wavelength of 520.8±13.5 nm for these cells [32].

Controls consisted of exposure of IGF-1R low-expressing MDA-MB-468 human breast adenocarcinoma cells[43, 46] to anti-IGF-1R nanosphere conjugates, IGF-1R expressing A549 cells exposed to IgG1 Ab labeled silver nanospheres, and A549 cells unexposed to labels. Control experiments showed negligible increases in scattering, demonstrating statistically significant differences in scattering intensity from the labeled, expressing cells and confirming molecular specificity (Figure 5).

A third set of experiments were performed to demonstrate the molecular specificity of the HER-2 Ab 60 nm gold nanosphere conjugation protocol. SK-BR-3 human breast adenocarcinoma cells were confirmed to over-express HER-2 [44, 47] using ELISA and were found to have 439.30 ± 14.98 ng/ml, approximately 20× that of control cells (MDA-MB-468). The SK-BR-3 cells were exposed to the HER-2 nanosphere conjugates and hyperspectral data cubes were acquired for individual cells using the hyperspectral microscopy system. Scattering spectra were averaged over multiple cells to assess labeling (N=147). Spectral measurements determine an average peak scattering wavelength of 587.0±11.9 nm for these cells [32].

Controls consisted of exposure of HER-2 non-expressing MDA-MB-468 human breast adenocarcinoma cells to HER-2 Ab nanospheres conjugates, [47–49] HER-2 expressing SK-BR-3 cells exposed to IgG1 Ab labeled gold nanospheres, and SK-BR-3 cells unexposed to any labels. Control experiments showed negligible increases in scattering, demonstrating statistically significant differences in scattering intensity from the labeled, expressing cells and confirming molecular specificity (Figure 6). Figure 7 displays images of cells labeled with the three described NP labels.

5. Discussion

The ability to provide spectral agility offers unique capabilities for plasmonic nanoparticles as labels for molecular imaging. Here we have reviewed several aspects of the synthesis and functionalization\protocols to enable access to a range of spectral windows. For synthesis,

we have shown that the seed-mediated method is useful for generating anisotropic gold nanoparticles with a tunable resonance. Weakly reduced gold ions bind to CTAB-capped gold seeds to generate larger particles. CTAB acts as a direction guiding surfactant by preferentially binding to the {110} faces along the length of the nanorod[25]. This prohibits growth in the transverse direction, thereby facilitating anisotropic growth. We have demonstrated that the addition of $AgNO_3$ controls the mean aspect ratio of the GNR batch. Orendorff et al provide a possible mechanism to explain this behavior[50]. Silver ions tend to deposit faster to the {110} faces along the side of the nanorod than the {100} faces at either end. Coupled with the preferential binding of CTAB, $AgNO_3$ reduces growth in the transverse direction, thereby increasing the mean aspect ratio. However, there is a limit to the extent of this effect. In general a maximum aspect ratio of approximately 5 may be obtained when fabricating GNRs in the presence of $AgNO_3$ [51], considering the deposition of Ag_0 on the {100} faces at the end of the rods. While deposition is faster at the sides of the nanorod, Ag_0 does in fact bind to the ends at a slower rate. Therefore, the rate of nanorod growth on the longitudinal direction should be reduced if enough silver ions are present in the solution. This could lead to the limited aspect ratio observed. In fact, in the absence of $AgNO_3$, nanorods with aspects as large as 20 may be synthesized[51]. However, the yield of rods versus spheres in this case is worse than when using $AgNO_3$.

We have shown that a linear relationship exists between the nanorods' aspects ratio and peak resonant wavelength (Fig 3d). The extinction properties of the rods may therefore be predictably controlled through manipulating their lengths relative to their width. These experiments have shown the ability to finely tune the mean aspect ratio of GNRs through the variation of $AgNO_3$, thereby adjusting the resonance peak anywhere within the 600–700 nm range. Although the applications discussed in this paper utilize GNRs scattering in the visible range, these relationships should hold through the NIR region as well. This wide range of extinction peaks makes nanorods a potential contrast agent in many applications. Shorter nanorods with resonant peaks in the visible range can be used to create molecular contrast in microscopy, while longer nanorods in the NIR range may be used in other modalities such as optical coherence tomography (OCT)[31]. Furthermore, multiple types of nanorods may be used in multiplexed molecular imaging applications if the resonant peak of each batch of NPs is sufficiently separated from the others [52].

In this review, we have also presented methods for conjugating different species of plasmonic nanoparticles to various antibodies (EGFR, HER-2 and IGF1-R). The measured scattering intensities of cells expressing the targeted receptors were significantly higher than those for the control experiments, including non-specific nanoparticle- anti-IgG conjugates, indicating that the NP-antibody conjugates exhibit molecularly specific binding. Therefore, measurements of NP scattering intensity may be used to determine a cell's expression level of a certain receptor[21]. Furthermore, multiplexed conjugated nanoparticles with separable spectral scattering characteristics can be utilized to develop an immunoassay of multiple receptors[32]. Plasmonic nanoparticles provide specific molecular contrast labeling with advantages over fluorophores and quantum dots for live cell labeling.

Simple detection of receptors is not the only application for antibody conjugated NPs. As previously mentioned, the peak resonant wavelength of an NP is dependent on the refractive index of the surrounding medium, among other factors. Therefore, the refractive index within a cell may be determined by measuring this peak, giving that the NPs geometry is already known[18, 53]. Changes in the cells refractive index may indicate fluctuations in ion concentration or the activation of cell signaling pathways. Thus, measuring changes in an NP's peak resonant wavelength can provide information on cellular dynamics.

Plasmonic nanoparticles can also be used in pairs to serve as molecular rulers. As two gold NPs approach one another, the plasmon oscillations couple to drive each other more so than the EM-wave would alone. This process, known as plasmon coupling, results in a redshifted resonance peak with higher amplitude compared to the single NP. This effect is amplified as the separation between the particles decreases. Furthermore, the effects of plasmon coupling are polarization dependent, relative to the axis between the two particles. Using techniques such as polarization mapping[54], the effects of plasmon coupling can be separated from other factors such as the surrounding dielectric medium. This allows for one to infer both the local refractive index and the spacing between two NPs. This is useful in examining cellular processes such as receptor dimerization [53].

6. Conclusions

Gold and silver nanoparticles are useful in biomedical imaging applications due to the enhanced absorption and scattering properties caused by LSPR. Furthermore, peak absorption and scattering wavelengths may be modified by using different materials or altering the size and shape of NPs during synthesis. While gold and silver spheres cover most of the visible range, gold nanorods may be tuned from the visible to near infrared wavelengths. This process may be controlled by simply changing the amount of $AgNO_3$ used during GNR synthesis. After conjugation with antibodies, NPs bind to targeted cellular recepetors with high specificity. This leads to higher intensities of scattered light measured from receptor expressing cells under darkfield microscopy. NPs can therefore be used to determine cell receptor expression levels. The unique properties of NPs can also provide other information, such as the refractive index within a cell, or the distance between two molecules. These various uses, along with NPs photostability and biocompatibility, present significant advantages over commonly used fluorophores and quantum dots.

Acknowledgments

This work was supported by the National Science Foundation (CBET-0651622). KS acknowledges support of NIH training grant (T32-EB001040). HP acknowledges support of the Lord Foundation Grant.

References

1. Kelly KL, et al. The Optical Properties of Metal Nanoparticles: The Influence of Size, Shape, and Dielectric Environment. J Phys Chem B. 2002; 107:668–677.
2. Lee K-S, El-Sayed MA. Gold and Silver Nanoparticles in Sensing and Imaging: Sensitivity of Plasmon Response to Size, Shape, and Metal Composition. J Phys Chem B. 2006; 110:19220–19225. [PubMed: 17004772]
3. Jain PK, et al. Calculated Absorption and Scattering Properties of Gold Nanoparticles of Different Size, Shape, and Composition: Applications in Biological Imaging and Biomedicine. J Phys Chem B. 2006; 110:7238–7248. [PubMed: 16599493]
4. Montet X, et al. Nanoparticle imaging of integrins on tumor cells. Neoplasia. 2006; 8(3):214–222. [PubMed: 16611415]
5. Montet X, et al. Tomographic fluorescence mapping of tumor targets. Cancer Research. 2005; 65(14):6330–6336. [PubMed: 16024635]
6. Bremer C, Tung CH, Weissleder R. In vivo molecular target assessment of matrix metalloproteinase inhibition. Nature Medicine. 2001; 7(6):743–748.
7. Xing Y, et al. Molecular profiling of single cancer cells and clinical tissue specimens with semiconductor quantum dots. International Journal of Nanomedicine. 2006; 1(4):473–481. [PubMed: 17722280]
8. Gao XH, et al. In vivo cancer targeting and imaging with semiconductor quantum dots. Nature Biotechnology. 2004; 22(8):969–976.

9. Alivisatos P. The use of nanocrystals in biological detection. Nature Biotechnology. 2004; 22(1): 47–52.
10. Mock JJ, Smith DR, Schultz S. Local refractive index dependence of plasmon resonance spectra from individual nanoparticles. Nano Letters. 2003; 3(4):485–491.
11. Nath N, Chilkoti A. A colorimetric gold nanoparticle sensor to interrogate biomolecular interactions in real time on a surface. Analytical Chemistry. 2002; 74(3):504–509. [PubMed: 11838667]
12. Nusz GJ, et al. Label-Free Plasmonic Detection of Biomolecular Binding by a Single Gold Nanorod. 2008:984–989.
13. Sonnichsen C, et al. Spectroscopy of single metallic nanoparticles using total internal reflection microscopy. Applied Physics Letters. 2000; 77(19):2949–2951.
14. Crow MJ, et al. Plasmonic flow cytometry by immunolabeled nanorods. Cytometry Part A. 2011; 79A(1):57–65.
15. Chen J, et al. Gold nanocages: Bioconjugation and their potential use as optical imaging contrast agents. Nano Letters. 2005; 5(3):473–477. [PubMed: 15755097]
16. Sokolov K, et al. Real-time vital optical imaging of precancer using anti-epidermal growth factor receptor antibodies conjugated to gold nanoparticles. Cancer Research. 2003; 63(9):1999–2004. [PubMed: 12727808]
17. Aaron J, et al. Plasmon resonance coupling of metal nanoparticles for molecular imaging of carcinogenesis in vivo. Journal Of Biomedical Optics. 2007; 12(3):034007–11. [PubMed: 17614715]
18. Curry A, Crow MJ, Wax A. Molecular imaging of epidermal growth factor receptor in live cells with refractive index sensitivity using dark-field microspectroscopy and immunotargeted nanoparticles. Journal Of Biomedical Optics. 2008; 13(1):014022-1-7. [PubMed: 18315380]
19. Gobin AM, et al. Near-infrared resonant nanoshells for combined optical imaging and photothermal cancer therapy. Nano Letters. 2007; 7(7):1929–1934. [PubMed: 17550297]
20. Loo C, et al. Gold nanoshell bioconjugates for molecular imaging in living cells. Optics Letters. 2005; 30(9):1012–1014. [PubMed: 15906987]
21. Crow MJ, et al. Molecular Imaging and Quantitative Measurement of Epidermal Growth Factor Receptor Expression in Live Cancer Cells Using Immunolabeled Gold Nanoparticles. Am J Roentgenol. 2009; 192(4):1021–1028. [PubMed: 19304709]
22. Frens G. Controlled Nucleation for the Regulation of the Particle Size in Monodisperse Gold Suspensions. Nature Physical Science. 1973; 241:20–22.
23. Hiramatsu H, Osterloh FE. A Simple Large-Scale Synthesis of Nearly Monodisperse Gold and Silver Nanoparticles with Adjustable Sizes and with Exchangeable Surfactants. Chemistry of Materials. 2004; 16(13):2509–2511.
24. Lee K-S, El-Sayed MA. Dependence of the Enhanced Optical Scattering Efficiency Relative to That of Absorption for Gold Metal Nanorods on Aspect Ratio, Size, End-Cap Shape, and Medium Refractive Index. J Phys Chem B. 2005; 109:20331–20338. [PubMed: 16853630]
25. Nikoobakht B, El-Sayed MA. Preparation and Growth Mechanism of Gold Nanorods (NRs) Using Seed-Mediated Growth Method. Chem Mater. 2003; 15:1957–1962.
26. Averitt RD, Westcott SL, Halas NJ. Linear optical properties of gold nanoshells. J Opt Soc Am B/. 1999; 16(10):1824–1832.
27. Zaman RT, et al. In vivo detection of gold nanoshells in tumors using diffuse optical spectroscopy. Ieee Journal of Selected Topics in Quantum Electronics. 2007; 13(6):1715–1720.
28. Nehl CL, Liao H, Hafner JH. Optical Properties of Star-Shaped Gold Nanoparticles. Nano Letters. 2006; 6(4):683–688. [PubMed: 16608264]
29. Hao F, et al. Plasmon Resonances of a Gold Nanostar. Nano Letters. 2007; 7(3):729–732. [PubMed: 17279802]
30. Agrawal A, et al. Quantitative evaluation of optical coherence tomography signal enhancement with gold nanoshells. Journal Of Biomedical Optics. 2006; 11(4):041121. [PubMed: 16965149]
31. Oldenburg AL, et al. Plasmon-resonant gold nanorods as low backscattering albedo contrast agents for optical coherence tomography. Optics Express. 2006; 14(15):6724–6738. [PubMed: 19516854]

32. Seekell K, et al. Hyperspectral molecular imaging of multiple receptors using immunolabeled plasmonic nanoparticles. JBO. 2011 p. Under Review.
33. Huang X, et al. Cancer Cells Assemble and Align Gold Nanorods Conjugated to Antibodies to Produce Highly Enhanced, Sharp, and Polarized Surface Raman Spectra: A Potential Cancer Diagnostic Marker. Nano Letters. 2007; 7(6):1591–1597. [PubMed: 17474783]
34. Loo C, Halas ALN, West J, Drezek R. Immunotargeted nanoshells for integrated cancer imaging and therapy. Nano Letters. 2005; 5(4):709–712. [PubMed: 15826113]
35. Curry A, Hwang WL, Wax A. Epi-illumination through the microscope objective applied to darkfield imaging and microspectroscopy of nanoparticle interaction with cells in culture. optics. Express. 2006; 14(14):6535–6542.
36. Eustis S, El-Sayed MA. Why gold nanoparticles are more precious than pretty gold: Noble metal surface plasmon resonance and its enhancement of the radiative and nonradiative properties of nanocrystals of different shapes. Chem Soc Rev. 2005; 35:209–217. [PubMed: 16505915]
37. Sonnichsen C, et al. Drastic Reduction of Plasmon Damping in Gold Nanorods. Physical Review Letters. 2002; 88(7):077402. [PubMed: 11863939]
38. Murphy CJ, et al. Gold Nanoparticles in Biology: Beyond Toxicity to Cellular Imaging. Account of Chemical Research. 2008; 41(12):1721–1730.
39. Draine BT, Flatau PJ. Discrete-dipole approximation for scattering calculations. J Opt Soc Am A. 1994; 11(4):1491–1499.
40. Draine, BT.; Flatau, PJ. User Guide to the Discrete Dipole Approximation Code DDSCAT 7.1. 2010. Available from: http://arXiv.org/abs/1002.1505v1
41. Perez-Juste J, et al. Optical Control and Patterning of Gold-Nanorod–Poly(vinyl alcohol) Nanocomposite Films. Advanced Functional Materials. 2005; 15(7):1065–1071.
42. Filmus J, et al. MDA-468, a human breast cancer cell line with a high number of epidermal growth factor (EGF) receptors, has an amplified EGF receptor gene and is growth inhibited by EGF. Biochemical and Biophysical Research Communications. 1985; 128(2):898–905. [PubMed: 2986629]
43. Riedemann J, et al. The EGF receptor interacts with the type 1 IGF receptor and regulates its stability. Biochemical and Biophysical Research Communications. 2007; 355(3):707–714. [PubMed: 17307140]
44. Lewis GD, et al. Differential responses of human tumor cell lines to antip185& lt;sup>HER2</ sup> monoclonal antibodies. Cancer Immunology, Immunotherapy. 1993; 37(4):255–263.
45. Gong Y, et al. High Expression Levels of Total IGF-1R and Sensitivity of NSCLC Cells In Vitro to an Anti-IGF-1R Antibody (R1507). PLoS ONE. 2009; 4(10):e7273. [PubMed: 19806209]
46. Ge L, et al. A -arrestin-dependent scaffold is associated with prolonged MAPK activation in pseudopodia during protease-activated receptor-2-induced chemotaxis. Journal of Biological Chemistry. 2003; 278(36):34418. [PubMed: 12821670]
47. Cuello M, et al. Down-regulation of the erbB-2 receptor by trastuzumab (herceptin) enhances tumor necrosis factor-related apoptosis-inducing ligand-mediated apoptosis in breast and ovarian cancer cell lines that overexpress erbB-2. Cancer research. 2001; 61(12):4892. [PubMed: 11406568]
48. Kramer-Marek G, Kiesewetter DO, Capala J. Changes in HER2 Expression in Breast Cancer Xenografts After Therapy Can Be Quantified Using PET and 18F-Labeled Affibody Molecules. J Nucl Med. 2009; 50(7):1131–1139. [PubMed: 19525458]
49. Hancock M, et al. A monoclonal antibody against the c-erbB-2 protein enhances the cytotoxicity of cis-diamminedichloroplatinum against human breast and ovarian tumor cell lines. Cancer research. 1991; 51(17):4575. [PubMed: 1678683]
50. Orendorff CJ, Murphy CJ. Quantitation of Metal Content in the Silver-Assisted Growth of Gold Nanorods. J Phys Chem B. 2006; 110(9):3994–3998.
51. Sau TK, Murphy CJ. Seeded High Yield Synthesis of Short Au Nanorods in Aqueous Solution. Langmuir. 2004; 20:6414–6420. [PubMed: 15248731]
52. Yu C, Nakshartí H, Irudayaraj J. Identity Profiling of Cell Surface Markers by Multiplex Gold Nanorod Probes. Nano Letters. 2007; 7(8):2300–2306. [PubMed: 17602538]

53. Crow MJ, et al. Monitoring of Receptor Dimerization Using Plasmonic Coupling of Gold Nanoparticles. ACS Nano. p. Under Review.

54. Crow MJ, Seekell K, Wax A. Polarization mapping of nanoparticle plasmonic coupling. Optics Letters. 2011; 36(5):757–759. [PubMed: 21368973]

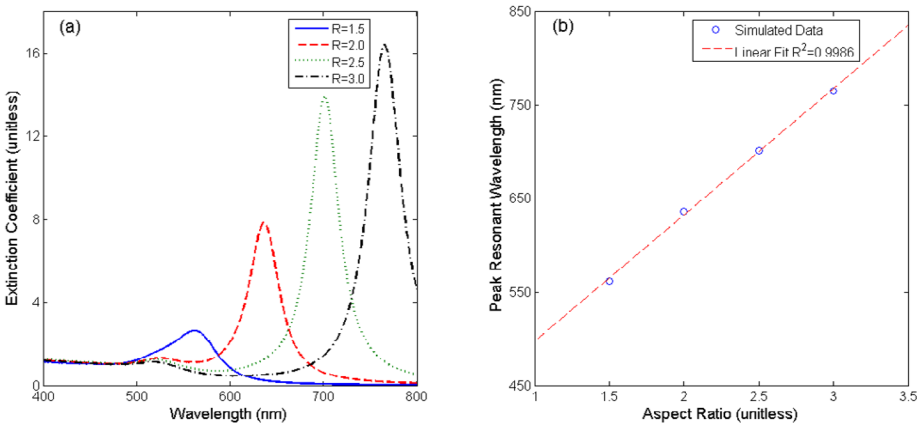

Figure 1.
DDSCAT simulations of GNRs. Example extinction spectra of GNRs with constant width and varying aspect ratio (a). Plot of the linear relationship between aspect ratio and peak resonant wavelength (b).

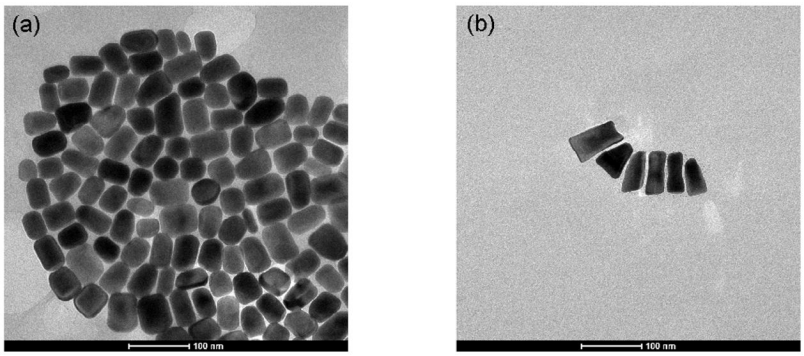

Figure 2.
Example TEM images of GNRs. Mean aspect ratio of 1.47±0.26 (a). Mean aspect ratio of 1.96±0.55 (b).

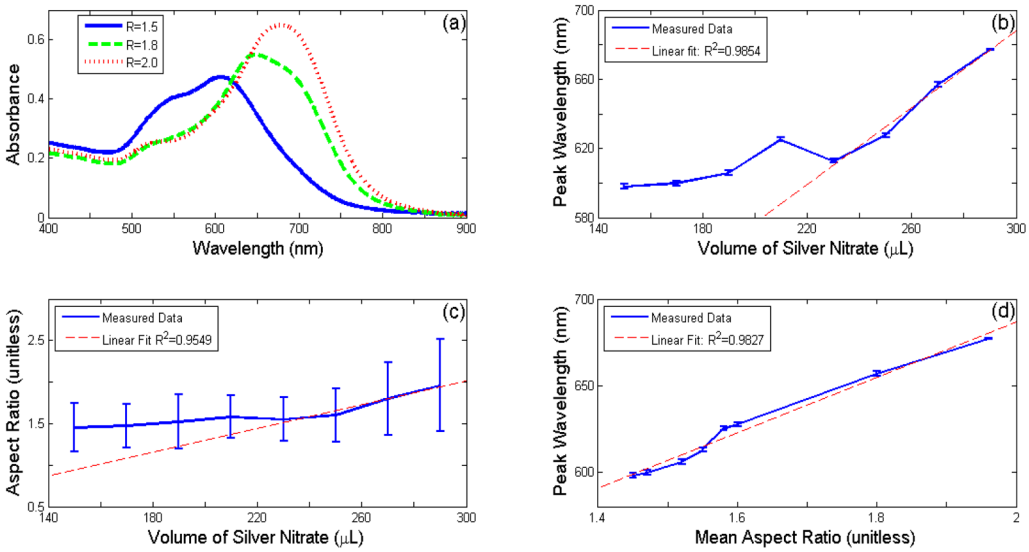

Figure 3.

Results of seed-mediated GNR synthesis with varying amounts of $AgN0_3$. Example absorption spectra of batches of GNRs with different aspect ratios (a). Longitudinal peak resonance wavelength versus volume of $AgNO_3$ (b). Aspect Ratio versus volume of $AgNO_3$ (c). Longitudinal peak resonance wavelength versus mean aspect ratio (d).

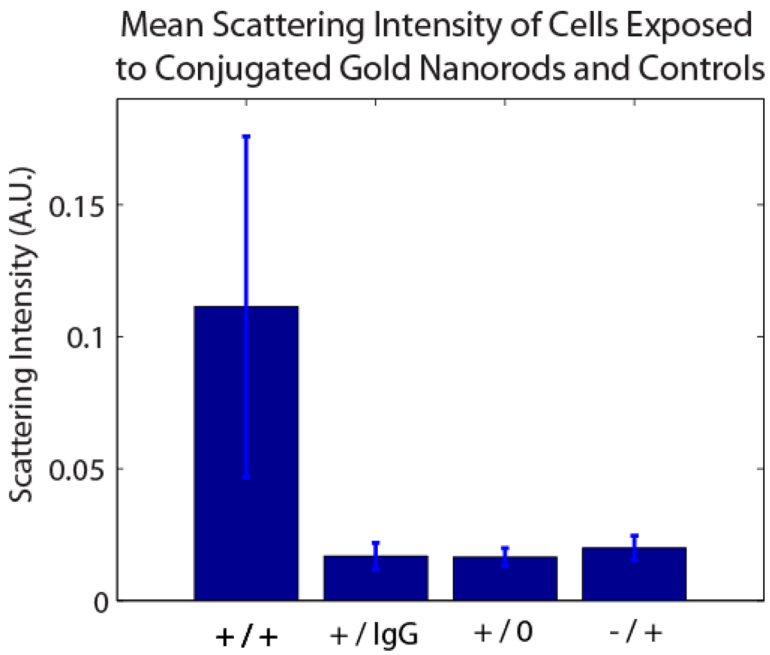

Figure 4.
Mean scattering intensity of 0.111 +/− 0.065 for EGFR expressing MDA-MB-468 cells exposed to anti-EGFR nanorods (+/+), 0.017 +/− 0.005 for MDA-MB-468 cells exposed to IgG Ab nanorods (+/IgG), 0.017 +/− 0.004 for MDA-MB-468 cells unexposed to conugates, and 0.020 +/− 0.005 for EGFR non-expressing MDA-MB-453 cells exposed to anti-EGFR nanorods.

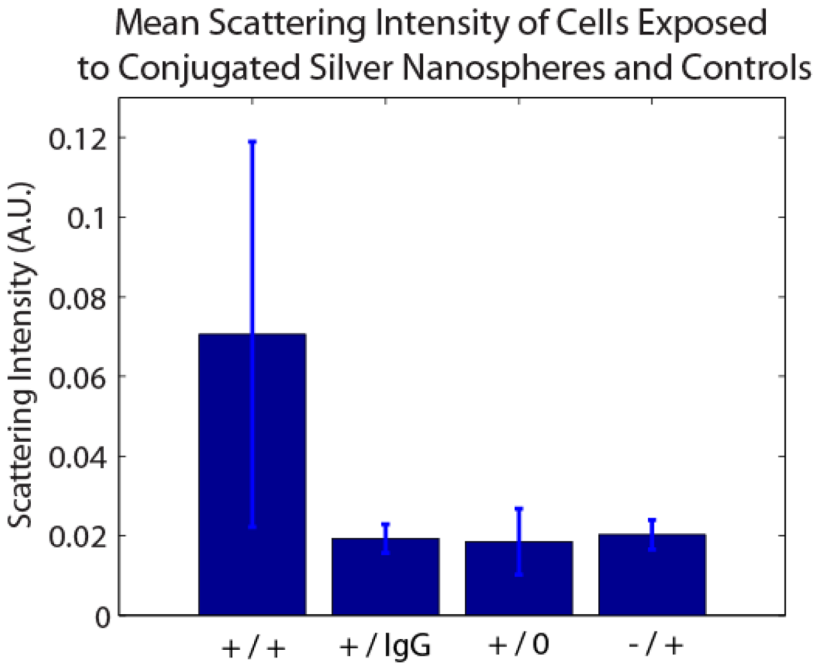

Figure 5.

Mean scattering intensity of 0.071 +/− 0.048 for IGF-1R expressing A549 cells exposed to anti-IGF-1R nanospheres (+/+), 0.019 +/− 0.004 for A549 cells exposed to IgG Ab nanospheres (+/IgG), 0.019 +/− 0.008 for A549 cells unexposed to conugates, and 0.020 +/− 0.004 for IGF-1R low-expressing MDA-MB-468 cells exposed to anti-IGF-1R nanospheres.

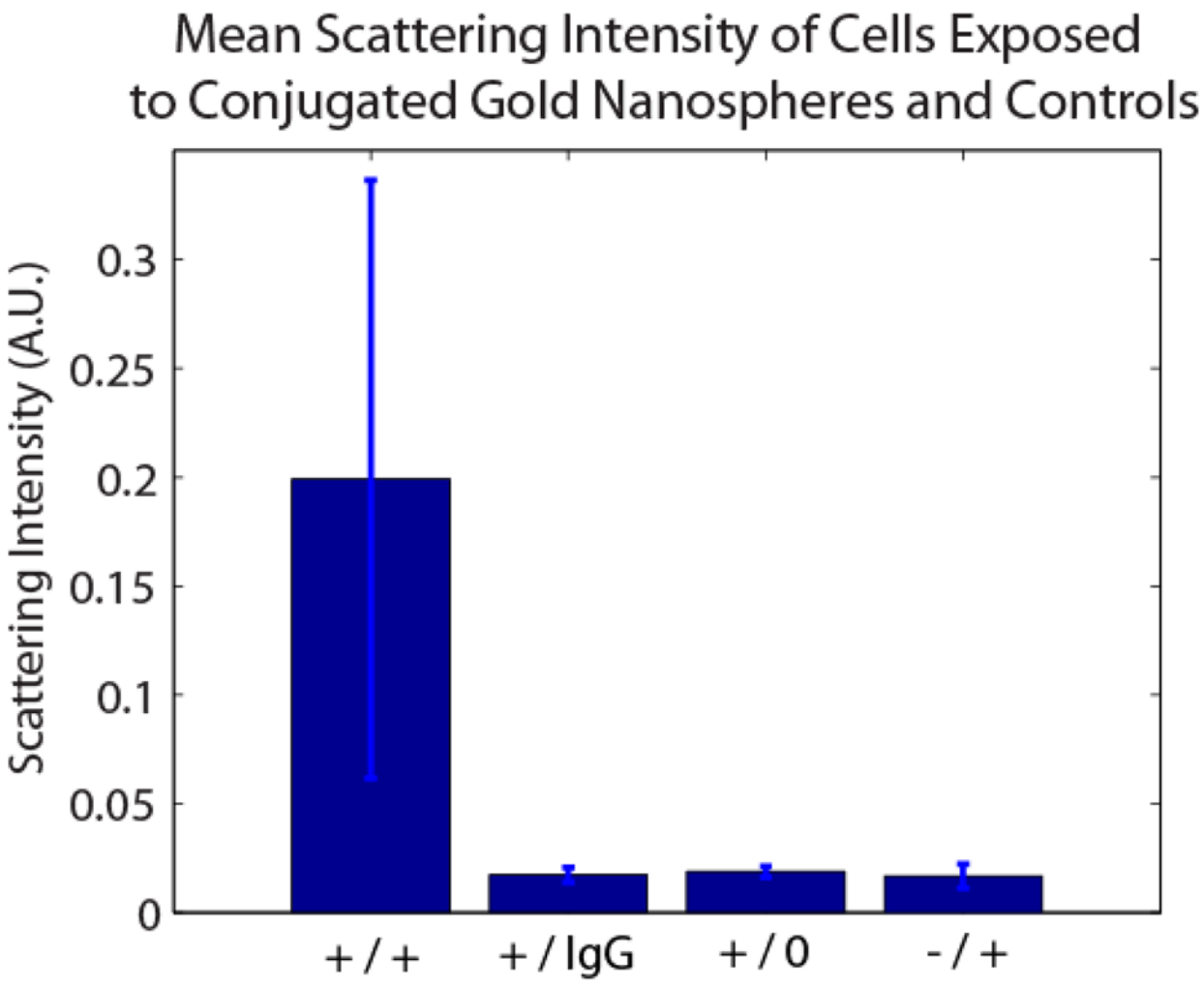

Figure 6.
Mean scattering intensity of HER-2 expressing SK-BR-3 cells exposed to HER-2 Ab nanospheres (+/+), SK-BR-3 cells exposed to IgG Ab nanospheres (+/IgG), SK-BR-3 cells unexposed to conugates (+/0), and HER-2 non-expressing MDA-MB-468 cells exposed to HER-2 Ab nanospheres (−/+).

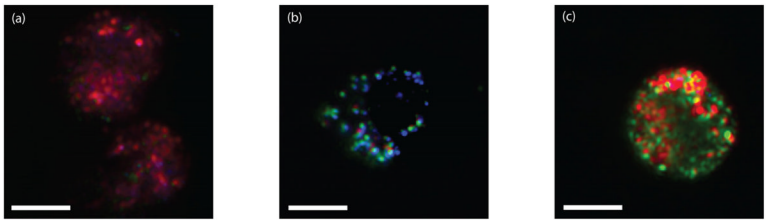

Figure 7.
RGB images of cells labeled with antibody conjugated NPs. EGFR+ MDA-MB-468 cells labeled with anti-EGFR gold nanorods (a). IGF-1R+ A549 cells labeled with anti-IGF-1R silver nanospheres (b). HER-2+ SKBR-3 cells labeled with HER-2 Ab gold nanospheres (c). Scale bars = 10 μm